

PAPER • OPEN ACCESS

## A Method to Incorporate Grain Boundary Strength and its Effects on Plastic Deformation in FCC Polycrystals

To cite this article: W Muhammad *et al* 2020 *IOP Conf. Ser.: Mater. Sci. Eng.* **967** 012026

View the [article online](#) for updates and enhancements.

You may also like

- [Plastic deformation and strengthening mechanism of FCC/HCP nano-laminated dual-phase CoCrFeMnNi high entropy alloy](#)  
Cheng Huang, Yin Yao, Xianghe Peng et al.
- [A comparison of different continuum approaches in modeling mixed-type dislocations in Al](#)  
Shuozhi Xu, Lauren Smith, Jaber R Mianroodi et al.
- [Dependence of equilibrium stacking fault width in fcc metals on the -surface](#)  
A Hunter, R F Zhang, I J Beyerlein et al.



**ECS**  
The  
Electrochemical  
Society  
Advancing solid state &  
electrochemical science & technology

**DISCOVER**  
how sustainability  
intersects with  
electrochemistry & solid  
state science research

# A Method to Incorporate Grain Boundary Strength and its Effects on Plastic Deformation in FCC Polycrystals

W Muhammad<sup>1,2</sup>, A P Brahme<sup>1</sup>, J Kang<sup>2</sup>, E Cyr<sup>1</sup>, D S Wilkinson<sup>3</sup> and K Inal<sup>1</sup>

<sup>1</sup> Department of Mechanical and Mechatronics Engineering, University of Waterloo, Waterloo, Ontario, N2L 3G1, Canada

<sup>2</sup> CanmetMATERIALS, 183 Longwood Road South, Hamilton, Ontario, L8P 0A5 Canada

<sup>3</sup> Department of Materials Science and Engineering, McMaster University, 1280 Main Street West, Hamilton, Ontario, L8S 4L7 Canada

Email: kinal@uwaterloo.ca; jidong.kang@canada.ca

**Abstract.** A three-dimensional (3D) crystal plasticity finite element method (CPFEM) is developed to investigate the effect of grain boundary strength on heterogeneous strain partitioning in FCC polycrystals. The proposed method incorporates electron backscatter diffraction (EBSD) maps into finite element analyses. The numerical analysis accounts for crystallographic texture, its evolution and 3D grain morphologies. Furthermore, grain boundaries are also mapped with a special finite element framework that allows material properties to be assigned to the grain boundaries. The material parameters and the grain boundary strengths are obtained by calibration to experimental uniaxial tension curves for single and polycrystals. Numerical simulations of uniaxial tension are performed and the effects of grain boundary strength on the onset of non-uniform deformation is investigated. The predicted local strain evolution is compared with corresponding experimental results from digital image correlation (DIC) measurements of an AA5754 aluminium sheet. The results showed that an excellent agreement was reached when the grain boundary properties were set so that the hardness was five times that of the average polycrystal response.

## 1. Introduction

Majority of the engineering materials of interest are polycrystalline in nature, consisting of several grains having different crystallographic orientations. Understanding the role of different contributing factors that are responsible for the overall macroscopic behaviour of these materials is of critical importance. These factors include response of each individual crystals/grain, the effect of grain boundaries as well as the effect on each grain due to the neighbouring grains. The simplest approach is to consider the polycrystal as an aggregate of the individual grains and completely ignore the effect of the neighbours. Classical approaches include enforcing either equal strain on each crystal as the polycrystal [1] or equal stress [2]. Thereafter, several approaches have been proposed. With the increase in the computing power, models that incorporate the crystal plasticity theory into the finite element formulation (CPFEM) have been the choice to capture these and other effects [3-5]. The CPFEM models enforce continuity and compatibility at the elemental level and have been used to successfully predict the mechanical properties as well as texture evolution during deformation for various polycrystalline systems such as FCC, BCC and HCP. A comprehensive review article by Roters et al. [6] provides an excellent overview of this approach.

Crystal plasticity theory accounts for the anisotropic behaviour of each grain based on its crystallographic orientation. This allows for non-uniform stress and strain distributions to be predicted



Content from this work may be used under the terms of the [Creative Commons Attribution 3.0 licence](https://creativecommons.org/licenses/by/3.0/). Any further distribution of this work must maintain attribution to the author(s) and the title of the work, journal citation and DOI.

as well as provides new insights on the influence of deformation mechanisms on localized deformation and failure. There have been many cases of crystal plasticity being used to study a range of material instabilities. To name a few: Peirce et al. [3] used crystal plasticity to predict shear bands in tensile single crystals. Wittridge and Knutsen [7] investigated surface roughness in aluminium alloys using a polycrystalline model. Dao and Li [8] and more recently Muhammad et al. [9-10] used crystal plasticity to predict crack initiation and propagation during bending of aluminium polycrystals. Potirniche et al. [11] used crystal plasticity to investigate void growth and coalescence in single crystals. Crystal plasticity has been used to predict the anisotropic behaviour of single crystals very accurately [12]. A set of material parameters can be fit to a single crystal orientation, which in turn can be used to predict the response of other orientations. However, in most cases the material parameters obtained from single crystal data need to be modified to match the polycrystalline response. There have been few works that try to solve this problem. Lim et al. [13] used single crystal continuum constitutive equations with a two scale (grain scale and meso scale) scheme to incorporate the effect of grain boundaries for larger grains. Kluseman et al. [14] used single crystal results to get the material parameters and combined them with size effect due to lack of grain size homogeneity to match deformation behaviour of thin sheets of Fe-3%Si. Cheong and Busso [15] investigated the effect of grain misorientation as well as strain hardening to match the polycrystal behaviour using single crystal material properties. Most of these works use data measured from oligo crystalline samples (samples with several grains covering the gage section) to validate and test their models. These microstructures provide an excellent opportunity to study grain scale plasticity [16-17].

In the literature, most of the existing crystal plasticity models do not have any special calculation or consideration at the grain boundary; they merely represent the boundary by having two neighbouring elements of different orientations [18-21]. Some models have been proposed where cohesive zone elements have been placed along the grain boundaries to account for small amounts of grain boundary slip, fracture, and grain boundary accommodation [22-23]. Lim et al. [13] introduced a model that uses dislocation density-based crystal plasticity in combination with 2D planar elements at the grain boundaries which act as a membrane to control dislocation transfer between neighbouring grains. This approach, in conjunction with the limited slip transfer through the boundary allows the model to predict the dislocation pileup seen in experimental observations and predict the characteristics seen in the grain boundary affected zone. Even though the grain boundary is a planar interface the mismatch of lattice structure at the grain boundary impedes dislocation motion causing dislocation pileup. This dislocation pileup can affect the material properties surrounding the grain boundary. Grain boundary affected zones have been shown to typically extend several micrometres into the grain [24].

The primary goal of this work is to incorporate the effect of grain boundaries into the CPFEM framework that will allow for inclusion of the associated strain inhomogeneity and material strengthening effect. In the first part of this work a method to incorporate the effect of boundaries will be proposed and validated using the DIC data as well as the polycrystalline flow curves provided by Zhu et al. [25] on large grained AA5754 sheets. The grain boundary affected zone will be identified and modelled as 3D elements with the element thickness equal to the grain boundary affected zone. In the next part the effect of boundary roughness on the overall material response will be studied.

## 2. Experimental procedures

### 2.1. Large grained AA5754 sample

Zhu et al. [25] created a large grained aluminum sample with two layers of columnar grains. The authors studied the deformation heterogeneity and strain localization and compared strain concentrations and correlated them to Taylor and Schmid factors. The advantage of the columnar structure is that 2D EBSD scans can be used to establish the 3D material microstructure. Since the sample consist of two layers, a scan from each side of the sheet is required and the structure can be made with the assumption that the two layers interface at the center of the sheet thickness. The sample identified as Sample A in Zhu et al. [25] will be reanalyzed and used in this work to generate the 3D material microstructure. The microstructure measured on both sides of the gauge area is shown in Figure 1 (a) has 12 grains and (b)

has 15 grains. The electron backscatter diffraction (EBSD) measurements were made to obtain the crystallographic orientation of the grains. A step size of 15  $\mu\text{m}$  was used for the measurements and multiple scans were obtained and were stitched together to obtain the overall large microstructure. The area shown in Figure 1 is slightly larger than the gage area. Note that the inverse pole figures presented here are rotated so that all directions are parallel to ND while the figures presented in Zhu et al. [25] have the directions parallel to RD. The EBSD dataset was cleaned using an iteration of neighbor confidence index (CI) of 0.2 to remove bad data points. The reader is referred to Zhu et al. [25] for further experimental details. The microstructure shows large grains with large variation in the grain size and an average grain size of 1.25 mm. These maps will be used to create the mesh that will be used in the CPFEM simulations.

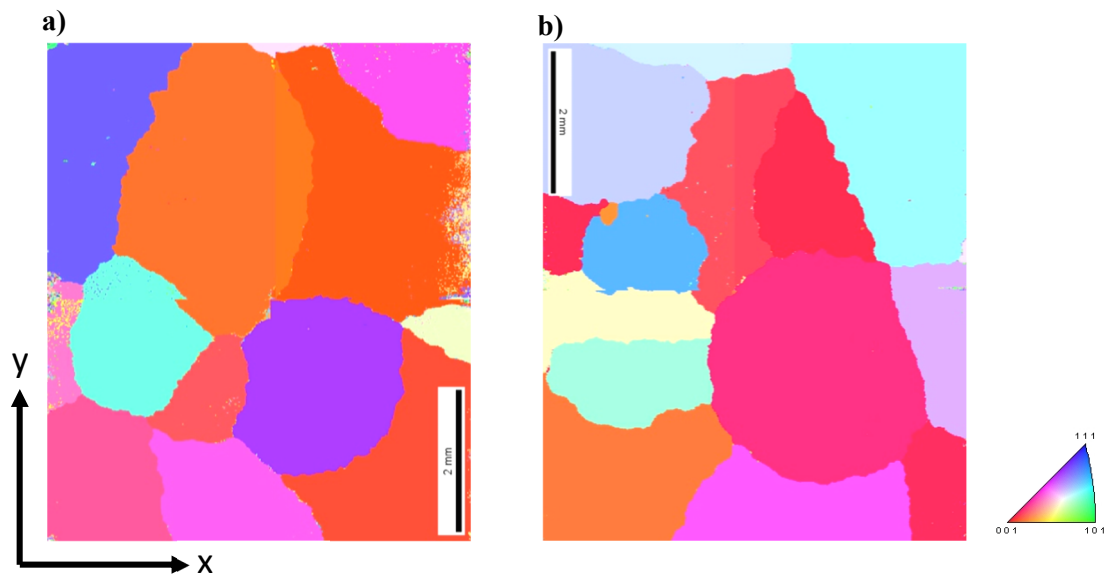


**Figure 1:** Inverse pole figure for large grained AA5754 aluminum polycrystal (a) Side A, (b) Side B.

The sample was then pulled in tension along the y-direction shown in Figure 1. The tensile tests were performed at a strain rate of  $2.7 \times 10^{-3}/\text{s}$  and the DIC images were recorded every 2s during the tensile test. The deformed speckled patterns were processed using the Aramis<sup>®</sup> software package and a regular grid of nodes was established as well as nodal movements throughout the test. As the DIC data is very sensitive to speckle pattern and image quality, there are some regions within images that are processed with lesser degree of confidence than the bulk of the image. These regions of “bad data” are filtered out and removed. The DIC data is further processed to plot the effective strain contour maps as shown in Figure 2. The applied strain at this point is 14%. This data is later used for comparison with simulated results. The tensile stress-strain response was also measured and is shown in Figure 3. The yield stress is approx. 50 MPa and the material shows significant work hardening prior to failure.

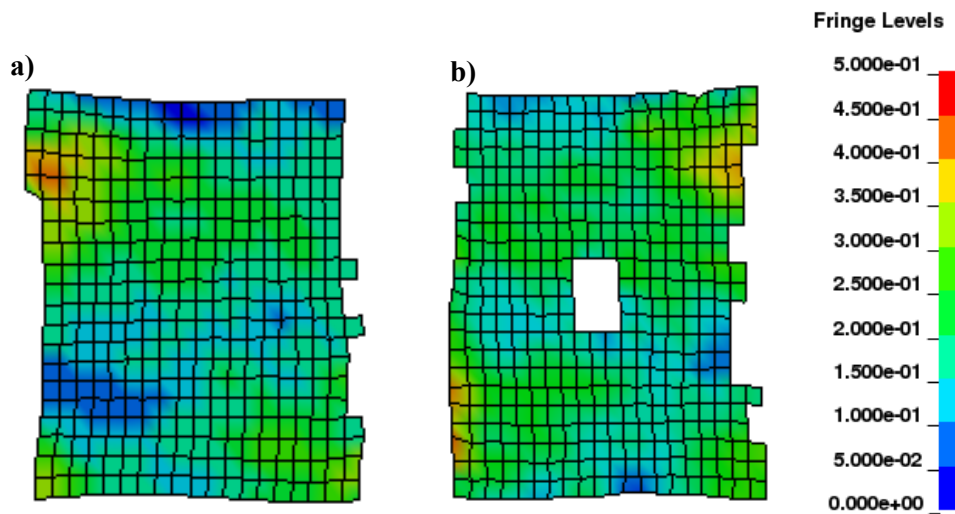


**Figure 2:** Experimental DIC measured effective strain maps for (a) Side A and (b) Side B of the specimen's gauge region at 14% strain for AA5754 aluminum polycrystal.

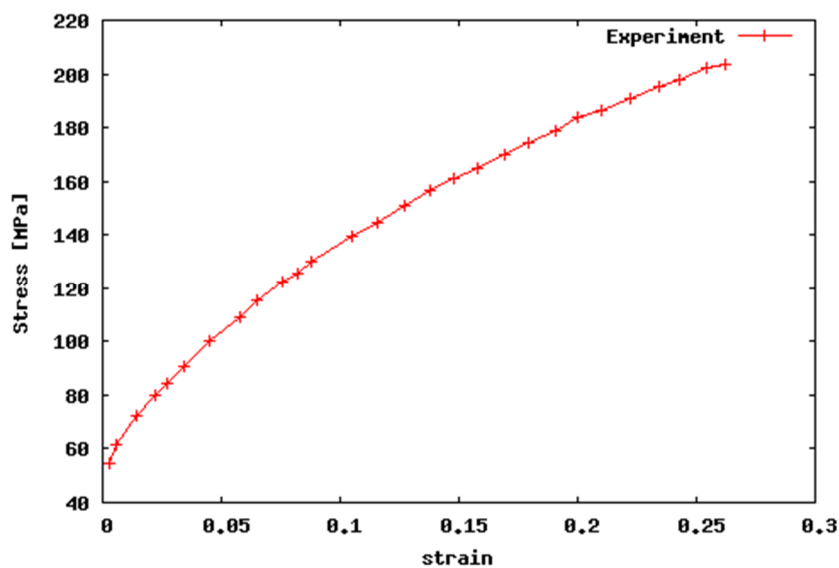


**Figure 3:** Experimentally measured stress vs. strain response for AA5754 aluminum polycrystal.

## 2.2. Single crystal data

Inoko et al. [26] presented aluminum single crystal data with tensile axis along  $\langle 001 \rangle$ ,  $\langle 111 \rangle$  and  $\langle 112 \rangle$  reproduced in Figure 4. This data on single crystals will be used to calibrate the material parameters for CPFEM simulations.

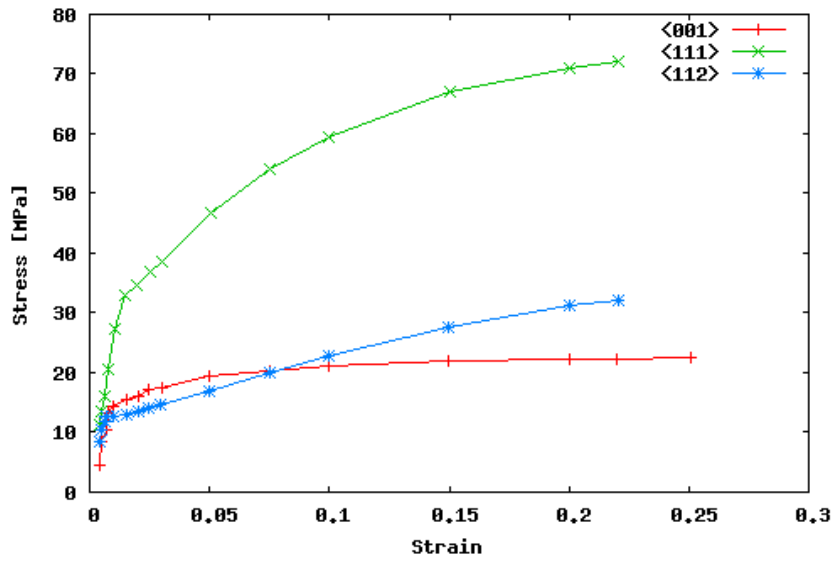


**Figure 4:** Aluminum single crystal tensile response along three different loading axes.

### 3. Numerical procedures

Crystal plasticity models are utilized on two levels. At the single crystal level; to identify the material parameters using single crystal constitutive model and at the polycrystal level; employing the Sample data A in Zhu et al. [25]. The single crystal CPFEM simulations employ single elements and are useful to assess the effect of crystallographic texture as the measured properties of single crystal data does not have any grain boundary effect. Two separate polycrystal models were developed to investigate the effect of grain boundaries. These will be discussed in detail in section 3.2.

#### 3.1. Constitutive model

The simulations performed for this paper use a rate dependent crystal plasticity theory formulated by Asaro and Needleman [27] implemented into the commercial FEM software LS-DYNA. For completeness, some important details of the formulation are summarized next.

The velocity gradient  $L^P$  is given by:

$$L^P = \sum_{\alpha=1}^{12} \dot{\gamma}^{\alpha} s^{\alpha} \otimes m^{\alpha} \quad (1)$$

where  $\dot{\gamma}^{\alpha}$  is the shear rate on the  $\alpha$ th slip system and  $s^{\alpha}$  and  $m^{\alpha}$  are the slip direction and slip plane normal, respectively. The shear rate is defined as:

$$\dot{\gamma}^{\alpha} = \dot{\gamma}_0^{\alpha} \left| \frac{\tau^{\alpha}}{g^{\alpha}} \right|^{1/m} \text{sgn}(\tau^{\alpha}) \quad (2)$$

where  $\dot{\gamma}_0^{\alpha}$ ,  $\tau^{\alpha}$  and  $g^{\alpha}$  are the reference shear rate, resolved shear stress and the hardness of the slip system  $\alpha$  and  $m$  is the rate sensitivity exponent. The slip system resistance term includes the particular choice of hardening rate  $\dot{g}^{\alpha} = \sum h_{\alpha\beta} \dot{\gamma}^{\beta}$ ;  $h_{\alpha\beta} = q_{\alpha\beta} h_{\beta}$  where  $h_{\alpha\beta}$  are the hardening moduli,  $q_{\alpha\beta}$  is the latent hardening matrix and  $h_{\beta}$  is the single slip hardening rate. The complete description of the constitutive model can be found in Rossiter et al. [28]. The work of Rossiter et al. [28] utilized a power law hardening. The only modification made to the constitutive model is the slip hardening model used for the single crystal material fit. The hardening model was modified to one that can be found in Harren et al. [29]:

$$h_{(\beta)} = h_s + (h_o - h_s) \text{sech}^2 \left\{ \left( \frac{h_o - h_s}{\tau_s - \tau_o} \right) \gamma_a \right\} \quad (3)$$

where  $h_o$  is the system's initial hardening rate,  $h_s$  is the system's asymptotic hardening rate,  $\tau_o$  is the critical resolved shear stress of the system,  $\tau_s$  is the saturation value of the shear stress, and  $\gamma_a$  is the accumulated slip. The reason for implementing this hardening law is that the single crystal experimental data found in Figure 4 displays a saturation hardening characteristic which is not obtainable using the power law hardening model used previously. The model that does not contain grain boundary zones and

single crystal material parameters still uses the original power law hardening model from Pierce et al. [30] as described in Rossiter et al. [28].

$$h_{(\beta)} = h_o \left( \frac{h_o \gamma_a}{\tau_0 n} + 1 \right)^{(n-1)} \quad (4)$$

$\tau_0$  is the critical resolved shear stress and  $n$  is the hardening exponent.

The constitutive model described above is used for the integration points in the single crystal and the polycrystal model, excluding the elements/integration points within the grain boundary zones. For the grain boundary zones, a simple elasto-plastic Mises plasticity constitutive model (LS-DYNA MAT24) is used. The stress vs. strain curve that is provided to the model is the experimentally measured stress vs. strain curve obtained from the tensile test modified by a scalar, which will be discussed in Section 3.3.2.

### 3.2. FE mesh generation

To study the effect of grain boundaries two separate meshes were generated. Both meshes were derived from the measured data from Zhu et al. [25]. The difference between the two meshes is the presence of grain boundary zones modeled with  $\sim 20 \mu\text{m}$  elements in one of them. The details of how the meshes are generated from the 2D EBSD maps are given next.

The EBSD data was processed to clean any bad data points and each pixel was assigned a grain number to which it belonged. The map was then analyzed to generate a list of pixel pairs such that each pixel in the pair belonged to two different grains. For every such pair a node representing a boundary point on the grain boundary was placed between them. The maps were processed again where every possible region of  $2 \times 2$  square pixels was analyzed and regions that contained pixels from 3 or more different grains were identified. A node representing a triple point was placed in the center of each of these  $2 \times 2$  regions. Once all the grain boundary points and triple points were identified in the map, the mesh for the grain boundary zone was constructed in the following manner. A piece of boundary was considered to be series of nodes separating two grains joining two triple points. Starting with a triple point at one end of the boundary, a series of bar elements was created connecting each boundary nodes along a boundary until the triple point on the opposite end of the boundary. This procedure was repeated for all boundaries. The result was a map of the grain boundaries consisting of 1-D bar elements. Since the sample consists of 2 separate layers of grains, the procedure for mapping the boundaries was conducted for both sides and then overlaid to produce a single map that contained outlines of all the grain boundaries on both layers of grains. The reason for combining the two layers of grain boundaries onto a single mesh is that when the final mesh is created, the elements and nodes at the interface between the two layers of grains need to match completely.

Once the system of bar elements representing the grain boundaries was completed, the 2D region within each grain was then meshed with shell elements. At this point, the addition of grain boundary zones was performed and the two distinct meshes were produced separately. For the mesh that includes the grain boundary zone, the nodes that represent the grain boundary nodes were duplicated, separated by approximately  $20 \mu\text{m}$ , and a quadrilateral shell element was placed in the gap. This resulted in triangular holes in the mesh at each triple point, which were filled with triangular elements.

Both meshes were then extruded to the thickness of the sample. The regions representing each grain were then combined and assigned a unique part designation and the orientations of the grains as measured from EBSD were assigned to the elements. The grain boundary zone elements for the whole structure were treated as a single part and were assigned a conventional plasticity material model.

The first step after building the polycrystal meshes is to determine the material parameters to be used in the simulations. For the model with grain boundaries, the material parameters are fitted using the single crystal data (Section 3.3.1) while for the model without grain boundaries, the material parameters are determined using the data published by Zhu et al. [25]. Once these are determined the model behaviors are compared between the single crystal and polycrystal fits. Next grain boundary zones are assigned properties and the predictions (Section 3.3.2) are compared to the data published by Zhu et al. [25]. Once a satisfactory value for the grain boundary parameters is obtained two independent studies

are performed (i) investigating the effect of grain boundary roughness (Section 4.3) and (ii) effect of boundaries in a complex forming operation (Section 4.4).

### 3.3. Model Parameters

Since the goal of this work is to develop a method of modeling polycrystals that can account for grain boundary effect, first a system which has no grain boundaries (single crystal) should be studied. In the single crystal case, only the grain orientation affects the stress strain response. This allows the single crystal constitutive model to be fitted with published single crystal data. Section 3.3.1 presents the method for determination of single crystal parameters. Once the single crystal constitutive properties have been established, the grain boundary properties can be established using the macroscopic polycrystal response of the sample. For the model that does not contain grain boundary zones, the macroscopic polycrystal response can be used to fit the constitutive model to act as a comparison to evaluate the benefits of modeling grain boundary zones.

#### 3.3.1. Single crystal

In order to identify the appropriate material parameters for the crystal plasticity constitutive model, single crystal simulations were performed and compared with published single crystal aluminum data. The single crystal stress-strain response published by Inoko et al. [26] and reproduced in Figure 4 is used for the parameter determination. A single element simulation of uniaxial tension was setup in LS-Dyna and LS-Opt was used to perform a parametric study to identify the appropriate material parameters. This allows one to find the parameter set that simultaneously fits all the curves represented in Figure 4. Initially for determination of parameters for the single crystal data, the power law slip hardening (see Eqn.4) from Peirce et al. [30] was used. The problem that arose from using this slip hardening model was that it is not capable of reproducing the saturation effect observed in the <001> loading direction seen in Figure 4. In order to obtain a closer fit with the single crystal material data, the slip hardening model was modified to the model found in Harren et al. [29] presented in Eqn. 3. The material parameters obtained by the LS-Opt optimization were then checked in a single integration point, crystal plasticity, material simulator to ensure the predicted uniaxial tension results given by the fitted parameters are in good agreement with the experimental data and are independent of the FE model. The material parameters determined using this procedure are reported in the Table 1.

**Table 1:** Crystal plasticity constitutive model material parameters.

Parameter	$\dot{\gamma}_0$ (s <sup>-1</sup> )	$h_o$ (MPa)	$\tau_o$ (MPa)	$h_s$ (MPa)	$\tau_s$ (MPa)	$n$
With Boundary Zones (single crystal parameters)	0.001	86	1.94	6.4	10	N/A
Without Boundary Zones	0.001	700	15	N/A	N/A	0.4

#### 3.3.2. Polycrystals

Once the single crystal material parameters were identified, the polycrystal meshes developed in Section 3.2 can be used to fit the grain boundary response. Initially, a simulation using these material parameters that does not contain grain boundary zones was performed and the overall stress vs. strain response is given in Figure 5. When compared to the experimental stress vs. strain curve, the model without grain boundary zones far under predicts the material response. This is expected since the hardening due to the grain boundaries is not included in the model. The model containing grain boundary zones was then used where the grain boundary zones were assigned a piecewise phenomenological plasticity material model along with a flow stress curve. To obtain the flow stress curve for the phenomenological model, the overall macroscopic stress vs. strain response from the polycrystal experimental results (see Figure 3) was taken as the base for the curve. A parametric study using LS-Opt was performed where a scalar value was used to modify the flow stress curve given to the grain boundary zones. This scalar was tuned so that it gave the lowest mismatch between the model prediction and the measured flow data. The

results from the fitting revealed that when the experimental stress vs. strain curve used in the grain boundary zones is multiplied by a scalar of 5, the overall response of the polycrystal matches the experimental data, as shown in Figure 5. The implication of this result is that a 20  $\mu\text{m}$  zone which encompasses a grain boundary should have a response that is 5 times harder than that of the macroscopic response. Given the existence of dislocation pileups and lattice mismatch at grain boundaries, this finding is in line with expectations. The exact value of this “5 times harder” is subjective since the required hardness applied to the grain boundaries in a model would change depending on the width chosen for the grain boundary zones as well as the exact material flow curve. Another factor that will affect the hardness required in the grain boundary zones would be the single crystal data used for the crystal plasticity model parameters. The data used for this study is pure aluminum single crystal data. The polycrystal used in this work is an AA5754 alloy. The intra-granular material properties might be slightly different than those found for pure aluminum. Nevertheless, the goal of this research is to investigate the benefit of using this modelling approach and its effect on simulated results will be investigated.

In order to compare the modelling approach of using grain boundary zones proposed in this work, an additional polycrystal fit was performed using the previous technique of fitting the single crystal constitutive material parameters to achieve the macroscopic response of the polycrystal. For this model, the mesh that does not contain grain boundary zones was used for the LS-Opt parametric fitting. It was found that the power law slip-hardening model given in equation 2 gave a near perfect fit using the material parameters found in Table 1 for the model without grain boundary zones.

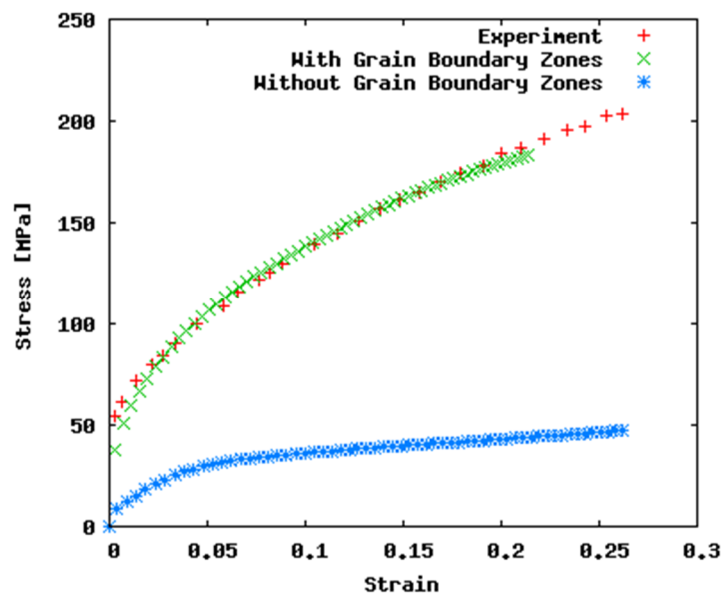
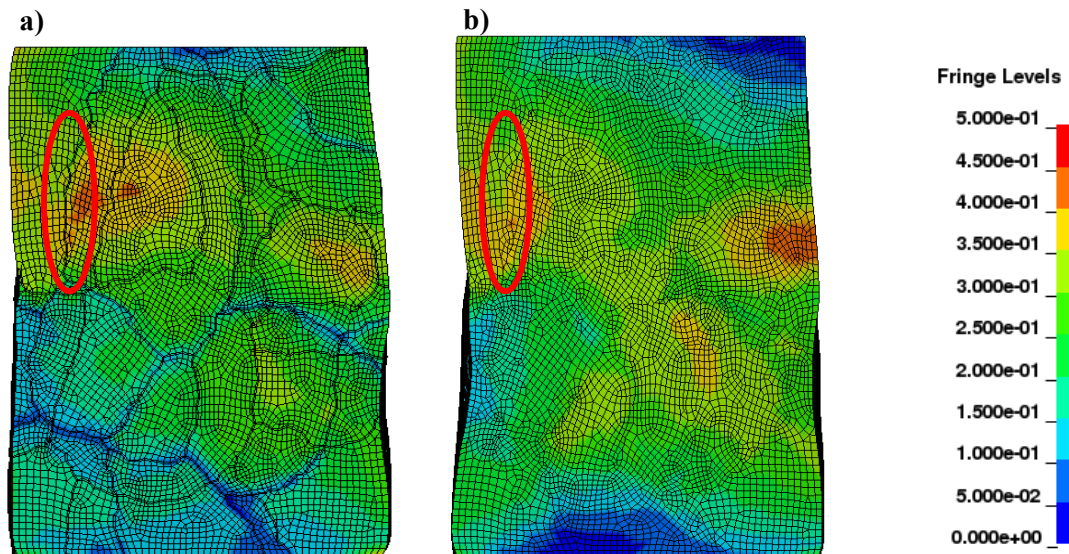


**Figure 5:** Stress vs Strain response for the polycrystal simulations using the single crystal fitted material response.

## 4. Results and discussion

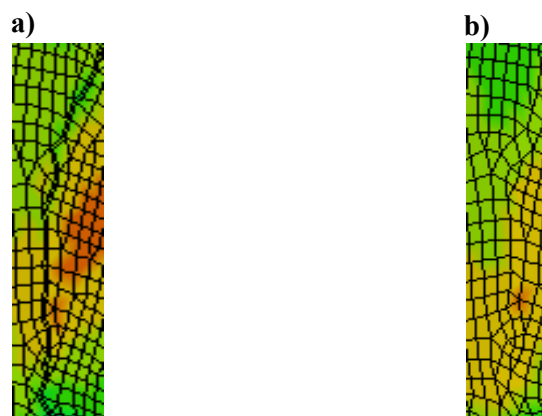
### 4.1. Uniaxial tension loading

Figure 6 (a) shows a deformed mesh at 14% strain for the model that includes grain boundary zones and Figure 6 (b) shows a deformed mesh with the same amount of strain for the model that does not have grain boundary zones (both having the same overall stress-strain behavior). Both these figures show the contours of effective strain and have the same scale. The two models show that the locations of hotspots are similar, but the value of effective strain is different in the two. For example, the highest strain is in the rectangular grain near the top left in the model with grain boundaries while the highest strain is within the equiaxed grain near the middle-right edge for the model without boundary zones. Both models show that the concentration is close to boundary between two grains.



**Figure 6:** Deformed effective strain maps for the numerical simulations (a) with and (b) without grain boundary zones at 14% applied strain.

A more detailed investigation of the deformed meshes presented in Figure 6 (a) and Figure 6 (b) shows that the hot spots are not exactly at the grain boundaries. Figure 7 provides a magnified view of the regions encircled in Figure 6 (a) and Figure 6 (b). In Figure 7 (a) the grain boundary zones/elements have lower strain than the surrounding region. The model without grain boundary zone has no such abrupt change in strain localization, as shown in Figure 7 (b). This is due to the substantial increase in the hardness that is given to the grain boundary zone in the material properties and is an artifact of the modeling approach. True grain boundaries exist as a gradient of material properties that changes as you get farther from the actual boundary interface. The DIC in situ strain measurement technique used to collect the experimental data is not at a sufficiently high resolution and magnification required to capture any low strain region such as that of a grain boundary zone.



**Figure 7:** Region of the model close to grain boundary in models (a) with grain boundary zone and (b) without grain boundary zone. These regions are encircled in red in Figure 6.

To validate and quantify the improvements in the model by adding grain boundary zones, the in-situ DIC strain measurements from the experimental tensile test were compared with the strain distributions measured from the simulations. The distributions were evaluated and quantified to establish that the addition of grain boundaries increased the accuracy of the model.

#### 4.2. Comparison with experimental results

The raw DIC data that was processed and presented in Zhu et al. [25] consists of a regular grid of surface points and their in-plane displacements for each side of the sample. This raw data was processed by creating a finite element mesh consisting of quadrilateral shell elements where the DIC surface points represents the nodes of the finite element mesh and the displacements of the points represent the nodal movements. The displacements were processed using quadrilateral element shape functions to create strain distribution maps. As mentioned in Section 2.1, Figure 2 shows an example of this mesh where the bad data points were at a minimum. Note that Figure 2 represents a smaller area than the one depicted in Figure 6 (a) and Figure 6 (b). Comparing Figure 2 (a) to Figure 6 (a) and Figure 6 (b), the hot spots and low spots of the model containing grain boundary zones are in better agreement with the DIC data. This qualitative comparison implies that the predictions of the model with grain boundary zones are more accurate. In order to quantify differences between the models and measured data, the models were processed to allow a direct comparison with the DIC data. The regular grid of DIC data points was overlaid onto the undeformed finite element mesh of the polycrystal. The surface nodes of the mesh that were the closest to the DIC data points were identified. The simulation results were data mined to extract the surface in-plane nodal movements of these nodes. A new data set was produced that matched the format of the initial DIC data which contained the locations of the mesh nodes closest to the DIC points and tracks their displacements throughout the simulation history. This new data set was then processed in the same manner as the initial DIC data to get a new distribution of strains that have the same resolution and direct element-to-element match with the DIC data.

A pixel-based Root Mean Squared (RMS) error was used to quantify the accuracy of the two models (with and without grain boundary zones).

$$E_{RMS} = \sum_{i=1}^N \sum_{j=1}^9 \left( (\varepsilon_{eff}^{sim})^2 - (\varepsilon_{eff}^{DIC})^2 \right)^{1/2} \quad (5)$$

where,  $i$  sums over all the pixels ( $N$ ),  $j$  sums over immediate neighborhood (first and second nearest neighbors)  $\varepsilon_{eff}$  is the effective strain. A square 9-pixel window was marched along each of the three data sets (DIC data set and the two models) in 1-pixel steps. For each step, the effective strain found within the window was averaged. For each window location, the average effective strain in the DIC data set was subtracted from the averaged strain in the models. Finally, an RMS error calculation was performed to obtain the total error from all locations. The RMS error is 0.122 for the model with boundary zones and the RMS error is 0.304 for the model without boundary zones. This is a significant improvement on the model results. By including the harder grain boundary zones, 60% of the error in the model has been eliminated.

#### 4.3. Mesh coarsening effects

The results from the previous section demonstrate that modeling the grain boundary zones has a positive effect on the results. Including the grain boundary zones in the model increases the computational time. The small elements that make up the zone elements cause a significant drop in the maximum time step size for the explicit FE calculations. In order to reduce the computation time of the model, it would be beneficial if the overall size of the grain elements could be increased to coarsen the mesh. The current size of the grain mesh is a function of the size of the small features found along the grain boundaries. If these features could be smoothed, then larger elements could be used along the grain boundaries and the overall mesh could be coarser. In order to smooth the grain boundaries, each triple point was identified, and a parabolic curve was fitted between the two triple points separating each section of the grain boundary. The curves were fitted to the grain boundaries using the statistical software MYSTAT to minimize the error between the parabolic curve connecting the triple points and the grain boundary nodes found from the EBSD data. A series of equal length bar elements were placed along the grain boundaries and the length of the bar elements could be varied to adjust the coarseness of the mesh. Once the bar elements were created, the remaining mesh was created using the same procedure as outlined in Section 3.2.

Two additional meshes were created, one where the same element coarseness as the original mesh was preserved (~80  $\mu\text{m}$  elements) and a second where the average element size was increased to ~180  $\mu\text{m}$ . The smoothed meshes along with the original mesh are presented in Figure 8. These meshes were

then subjected to tension similar to the original mesh using the same material properties identified previously. The uniaxial tensile stress vs strain response of these smoothed meshes along with the original mesh and the experimental data are shown in Figure 9. It shows that smoothing the grain boundaries did not significantly affect the macroscopic stress strain response of the model, however coarsening the elements did cause a change in the resulting stress vs. strain curve. Figure 10 shows the effective strain distributions for the three simulated meshes. Even though the overall strain distribution is similar when the grain boundaries are smoothed, the intensities of the strain hot spots are different. The coarse and smoothed meshes have the strain hot spots closer to triple junction points. Thus, the smoothing of the grain boundary and coarsening do have a significant effect on the overall predictions of the model.

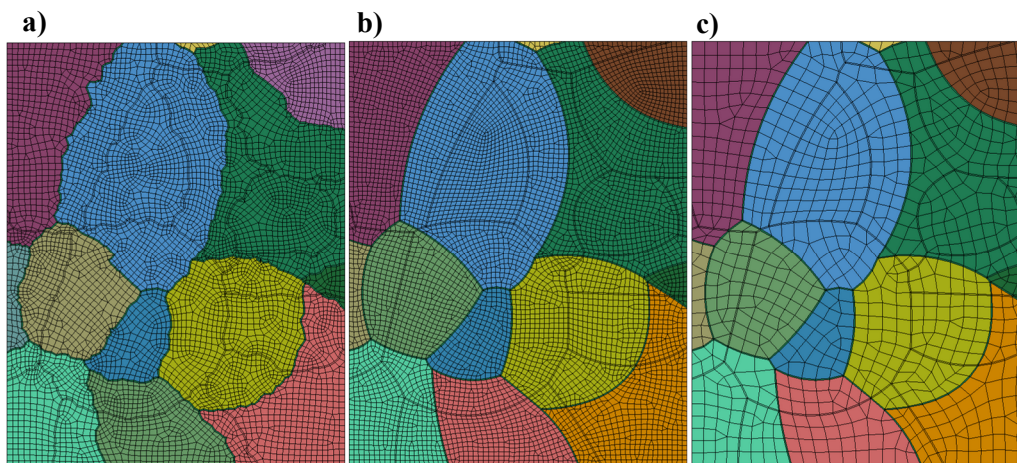


**Figure 8:** Finite element mesh with a) the original microstructure, (b) smoothed grain boundaries with the original element size ( $\sim 80 \mu\text{m}$ ), and (c) smoothed grain boundaries with coarsened element size ( $\sim 180 \mu\text{m}$ ).

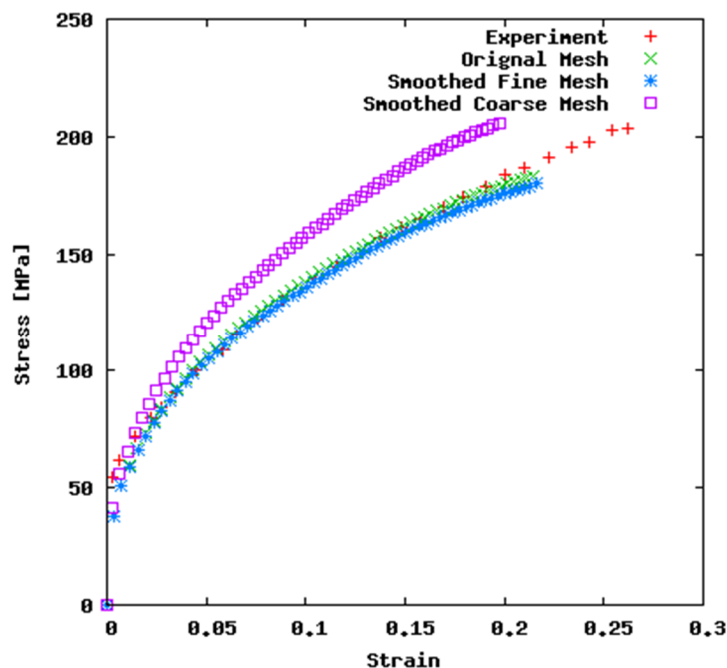


**Figure 9:** Stress vs Strain response for the polycrystal simulations comparing the effect of smoothing the grain boundaries and coarsening the mesh.

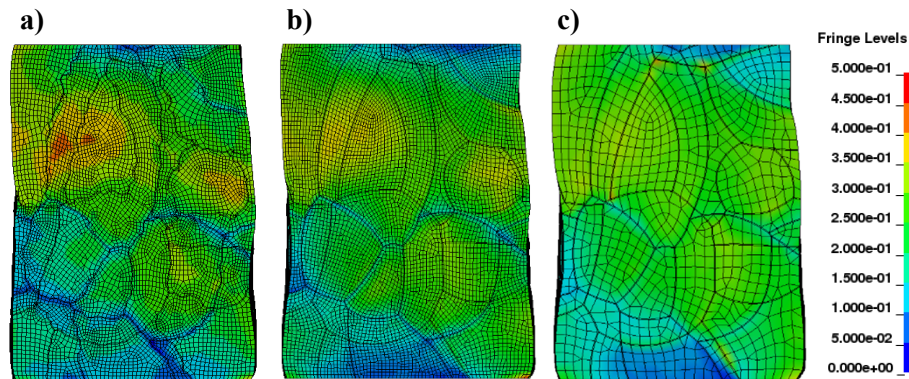


**Figure 10:** Effective strain distributions for the finite element mesh with a) the original microstructure, (b) smoothed grain boundaries with the original element size ( $\sim 80 \mu\text{m}$ ), and (c) smoothed grain boundaries with coarsened element size ( $\sim 180 \mu\text{m}$ ).

In this work, all grain boundary zones were treated as being identical, which might not be reflective as it is expected of boundaries with different grain boundary characters to have different response [24]. Also, this study treats the boundary zones as rectangular region of equal thickness ( $\sim 20 \mu\text{m}$ ) with hard cut-offs. In reality, this zone exhibits smoother transition, where the influence reduces as one moves farther away from the boundary towards grain centers [31]. Despite these, the models do indicate that the grain boundaries have a significant effect and can be used without the need of other approaches like Hall-Petch etc. to account for the higher hardening of polycrystalline materials as compared to single crystals.

## 5. Conclusions

A new modeling approach was developed to use single crystal material properties by fitting it to experimental data and translating it to polycrystal models. To achieve this, the grain boundaries were identified, and separate grain boundary zone was created. This zone was assigned separate material parameters. The predictions of the model were validated by comparing predicted results to measured DIC data. Based on the work presented, the following conclusions can be drawn:

- It is feasible to use single crystal constitutive behaviour and extend the predictions to polycrystal model by using separate properties for the grain boundary zone.
- The grain boundary zone has a large impact on the strain partitioning as it is harder than the grain centers and forces the matrix to accommodate more strain.
- Comparison with DIC data shows a 60% reduction in the total error between measured and predicted strain distributions when using the correct grain boundary properties.
- Coarsening of the mesh and smoothing of the grain boundaries had a significant effect on local strain distribution especially in vicinity of the triple junctions. This implies any attempt at speed up of the procedure using these techniques needs to be validated before use.

## Acknowledgements

This work was supported by the Natural Sciences and Engineering Research Council of Canada (NSERC) and General Motors of Canada through the Collaborative Research and Development (CRD) grant number CRDPJ401744-10.

## References

- [1] Taylor G I, 1934 *Proc. Roy. Soc. A.* **165** 362.
- [2] Sachs G, 1928 *Z. Ver. Dtsch. Ing.* **12** 134–136.

- [3] Peirce D, Asaro R J, and Needleman A, 1982 *Acta Metallurgica* **30** 1087-1119.
- [4] Asaro R J, 1983 In: *John W. Hutchinson and Theodore Y. Wu, Editor(s), Advances in Applied Mechanics, Elsevier* **23** 1-115.
- [5] Anand L, and Kalidindi S R 1994 *Mechanics of Materials* **17** 223-243.
- [6] Roters F, Eisenlohr P, Hantcherli L, Tjahjanto D, Bieler T R, and Raabe D 2010 *Acta Materialia* **58** 1152-1211.
- [7] Wittridge N J, and Knutsen R D 1999 *Materials Science and Engineering: A* **269** 205-216.
- [8] Dao M, and Li M 2001 *Philosophical Magazine A* **81**(8) 1997-2020.
- [9] Muhammad W, Kang J, Brahme A P, Ali U, Hirsch J, Brinkman H, Engler O, Mishra R K and Inal K 2019 *Materials Science and Engineering: A* **753** 179-191.
- [10] Muhammad W, Brahme A P, Ali U, Hirsch J, Engler O, Aretz H, Kang J, Mishra R K and Inal K 2019 *Materials Science and Engineering: A* **754** 161-177.
- [11] Potirniche G P, Hearndon J L, Horstemeyer, M F, and Ling, X W 2006 *International Journal of Plasticity* **22** 921.
- [12] Izadbakhsh A, Inal K, and Mishra R K 2010 *Computational Materials Science* **50** 571-585.
- [13] Lim H, Lee M G, Kim J H, Adams B L, and Wagoner R H 2011 *International Journal of Plasticity* **27** 1328-1354.
- [14] Klusemann B, Svendsen B, and Vehoff H 2012 *Computational Materials Science* **52**(1) 25-32.
- [15] Cheong, S, and Busso E P 2006 *Journal of the Mechanics and Physics of Solids* **54**(4) 671-689.
- [16] Raabe D, Sachtleber M, Zhao Z, Roters F, and Zaefferer S 2001 *Acta Materialia* **49**(17) 3433-3441.
- [17] Lim H, Carroll J D, Battaile C C, Buchheit T E, Boyce B L, Weinberger C R 2014 *International Journal of Plasticity* **60** 1-18.
- [18] Li S, Van Houtte P, and Kalidindi S R 2004 *Modelling and Simulation in Materials Science and Engineering* **12** 845-870.
- [19] Delannay L, Jacques P J, Kalidindi S R 2006 *International Journal of Plasticity* **22** 1879-1898.
- [20] Erinoshio TO, Cocks A C F, and Dunne F P E *International Journal of Plasticity* **50** 170-192.
- [21] Muhammad W, Brahme A, Kang J, Mishra R, and Inal K 2016 *E. Williams (Ed.) Light Metals 2016* 169-174.
- [22] Wei Y J, and Anand L 2004 *Journal of the Mechanics and Physics of Solids* **52** 2587 – 2616.
- [23] Sfantos G K, and Aliabadi M H 2006 *International Journal for Numerical Methods in Engineering* **69** 1590-1626.
- [24] Randle V, Hansen N, and Jensen D J 1996 *Philosophical Magazine A* **73**(2) 265-82.
- [25] Zhu G, Hu X, Kang J, Mishra R, and Wilkinson D 2011 *Materials Science and Engineering A* **528** 4187-4198.
- [26] Inoko F, Kashihara K, Tagami M, and Okada T 2010 *Materials Transactions* **51** 597-606.
- [27] Asaro R J, and Needleman A, 1985 *Acta Metallurgica* **33**, 923-953.
- [28] Rossiter J, Brahme A, Simha H, Inal K, and Mishra R K 2010 *International Journal of Plasticity* **26** 1702-1725.
- [29] Harren S, Lowe T.C, Asaro R J, and Needleman A 1989 *Philosophical Transactions of the Royal Society of London A* **328** 443-500.
- [30] Peirce D, Asaro R J, and Needleman A 1982 *Acta Metallurgica* **30** 1087-1119.
- [31] Mishra S, Pant P, Narasimhan K, Rollett A D, and Samajdar I 2009 *Scripta Materialia* **61**(3) 273-276.